Journal of Materials Chemistry C

ROYAL SOCIETY OF CHEMISTRY

PAPER

View Article Online
View Journal | View Issue



Cite this: J. Mater. Chem. C, 2026, 14, 357

# Probing structural and optical modulations in metal-ion co-doped gadolinium vanadate: a combined spectroscopic and diffraction study

Ahmed G. Attallah, †*[ab] Arzu Cosgun Ergene, †[c] Eric Hirschmann, [a] Maik Butterling,‡[a] Dmitry Busko,[c] Aditya Chauhan,[c] Bryce S. Richards [cd] and Andrey Turshatov *[c]

Upconversion (UC) luminescence enhancement in trivalent lanthanide-doped materials – particularly the ytterbium ($Yb^{3+}$)/erbium ($Yb^{3+}$) ion pair – remains challenging due to complex, interdependent mechanisms involving structural modifications and defect formation. Here, we present a systematic investigation of UC enhancement in relation to defect formation in $GdVO_4$:$Yb^{3+}$/$Er^{3+}$ microcrystals through strategic co-doping with optically inactive ions ($Sc^{3+}$, $Cd^{2+}$, $Zn^{2+}$). We employ a novel multi-technique approach combining positron annihilation lifetime spectroscopy (PALS) – to quantify vacancy-type defects in UC materials – with X-ray diffraction and photoluminescence quantum yield (PLQY) measurements to establish direct structure–defect–property relationships. Our results reveal that dopant valence and ionic radius dictate distinct defect formation patterns: isovalent $Sc^{3+}$ substitution primarily induces lattice contraction with minimal point defect generation, while aliovalent $Cd^{2+}$ and $Zn^{2+}$ doping creates extensive Gd vacancy networks through charge compensation mechanisms. Critically, we demonstrate that defect cluster size and spatial distribution, rather than total defect concentration, govern UC efficiency. $Zn^{3+}$ co-doping achieves a remarkable PLQY enhancement through progressive suppression of large vacancy clusters at grain boundaries, coupled with favorable redistribution of oxygen vacancies within crystallite interiors. In contrast, $Cd^{2+}$ doping, despite similar charge compensation requirements, produces extended defect clusters that act as efficient non-radiative quenching centers, limiting PLQY improvement. These findings establish defect engineering as a powerful strategy for UC optimization and provide a quantitative framework for rational design of high-efficiency lanthanide-based photonic materials.

Received 7th September 2025,
Accepted 5th November 2025

DOI: 10.1039/d5tc03342j

rsc.li/materials-c



## 1. Introduction

The quest for high-efficiency, multifunctional light-converting materials has directed considerable attention toward the development of advanced luminescent systems.[1,2] Within this context, upconversion (UC), a complex nonlinear optical process wherein two or more low-energy photons are converted into a singular high-energy photon,[3] has attracted significant attention.[4] UC materials, distinguished by their distinctive optical properties, have emerged as promising candidates with diverse applications in fields of bioimaging,[5–7] photovoltaics,[8,9] photocatalysis,[10,11] and anti-counterfeiting.[12] However, the efficiency of UC in most materials remains suboptimal, primarily owing to the weak absorption of sensitizer ions[13] and the nonradiative relaxation of excited states.[14–16] Consequently, various strategies have been developed to enhance UC luminescence, encompassing optimization of the host matrix,[17] modification of surface properties,[18] and the introduction of co-dopants.[19]

UC processes are commonly categorized into lanthanide ($Ln^{3+}$)-based UC, where emissive $Ln^{3+}$ ions play the central role.[20] Transition metal[21] and actinide ions[22] also exhibit UC capabilities together with a distinct category termed triplet–triplet annihilation UC.[23] However, this work focuses on the former. $Ln^{3+}$-based UC materials primarily rely on a robust solid inorganic matrix, such as glass, or a crystalline host

[a] Helmholtz-Zentrum Dresden-Rossendorf, Institute of Radiation Physics, 01328 Dresden, Germany. E-mail: a.elsherif@hzdr.de
[b] Physics Department, Faculty of Science, Minia University, 61519 Minia, Egypt
[c] Karlsruhe Institute of Technology (KIT), Institute of Microstructure Technology (IMT), 76344 Eggenstein-Leopoldshafen, Germany. E-mail: andrey.turshatov@kit.edu
[d] Karlsruhe Institute of Technology (KIT), Light Technology Institute (LTI), 76131 Karlsruhe, Germany
† Equal contribution.
‡ Present address: Reactor Institute Delft, Department of Radiation Science and Technology, Faculty of Applied Sciences, Delft University of Technology, Mekelweg 15, NL-2629 JB Delft, The Netherlands.

exemplified by metal fluorides, oxides, phosphates, or vanadates. These matrices are doped with either a single $Ln^{3+}$ ion – for example, $Er^{3+}$, which is then used for near-infrared (NIR, 1500 nm to NIR, 980 nm) UC[24] – or a combination of $Ln^{3+}$ ions, such as $Yb^{3+}$ as a sensitizer ion (980 nm excitation, which is then paired with an activator ions such as $Er^{3+}$ (green/red emission) $Tm^{3+}$ (blue/800 nm emission) or $Ho^{3+}$ (green emission).[25]

Among the host matrices, gadolinium vanadate ($GdVO_4$) stands out as a good host candidate for UC applications, valued for its high chemical stability, low phonon energy, and strong crystal field splitting.[19] $GdVO_4$ readily accommodates diverse lanthanide ion doping[26] and exhibits tunable UC emission colors under NIR excitation.[27,28] However, the efficiency of UC emission in the $GdVO_4$ host is hindered by constraints arising from concentration quenching and cross-relaxation processes intrinsic to activator ions. In addition, surface and defect induced quenching plays a dominant role when $GdVO_4$ nanocrystals are synthesized by co-precipitation or sol–gel methods.[29]

To overcome these limitations, metal-ion co-doping has been widely adopted as a strategy to enhance UC efficiency by tailoring the local structure, improving energy transfer efficiency, and reducing non-radiative losses. However, as previously noted, the enhancement mechanisms are often multifactorial and interdependent, making it difficult to isolate the contribution of individual structural changes.[30] Factors such as lattice strain, particle size, surface-to-volume ratio, phonon energy, local symmetry, and particularly crystal defects can each influence UC intensity, often in overlapping and nontrivial ways.[19]

Our previous work[19] on co-doping $GdVO_4$:$Yb^{3+}$/$Er^{3+}$ with $Zn^{2+}$ and $Sc^{3+}$ demonstrated significant UC enhancement *via* distinct mechanisms: $Zn^{2+}$ co-doping induced both lattice shrinkage and grain growth, leading to up to a 60-fold increase in UC intensity, whereas $Sc^{3+}$ introduced isovalent lattice contraction with relatively modest enhancement ($\sim$20$\times$ UC). These enhancements were attributed to a combination of structural stabilization and more efficient energy migration. However, in both cases, the explicit role of crystal defects – and their potential as non-radiative centers or sensitization sites – was not fully delineated due to simultaneous morphological changes.

Given the anticipated relationship between atomic-scale defect formation – induced by co-doping – and the evolution of UC luminescence in lanthanide-doped $GdVO_4$ crystals, this study aims to elucidate the respective roles of crystal defects and structural modifications. In this context, we propose a more comprehensive co-doping strategy that expands beyond $Zn^{2+}$ and $Sc^{3+}$ to include a set of optically inactive co-dopants with distinct physical and chemical characteristics. Specifically, we selected $Cd^{2+}$, $Bi^{3+}$, and $In^{3+}$, in addition to $Zn^{2+}$ and $Sc^{3+}$, to explore the influence of ionic radius, valence state, and intermediate compound behavior. This selection allows for systematic modulation of charge compensation, lattice volume, defect density, and particle size – while controlling for synthesis conditions by using the same co-precipitation route followed by high-temperature calcination (700–850 °C) to ensure uniform grain growth. A summary of these co-dopants, their corresponding intermediate phases, ionic radii, melting points, and dominant structural effects is provided in Table 1. Results for $Zn^{2+}$ and $Sc^{3+}$ are drawn from our previous study,[19] while new data for $Cd^{2+}$, $Bi^{3+}$, and $In^{3+}$ are presented herein. This table outlines the expected structural modifications induced by the ion co-doping and provides a foundation for our correlative analysis using a multi-technique approach combining positron annihilation lifetime spectroscopy (PALS) (to probe vacancy-type defects), X-ray diffraction (XRD) (to assess lattice distortion), and photoluminescence quantum yield (PLQY) (to quantify emission efficiency of luminescence).

PALS is a powerful, non-destructive technique for probing atomic-scale defects in solids.[31] Unlike surface-sensitive methods such as X-ray photoelectron spectroscopy (XPS), which typically investigate a few nanometers beneath the surface, source-based conventional PALS techniques can probe deeper sites. In these techniques, positrons, the antimatter counterparts of electrons, are emitted by a $^{22}Na$ radioisotope, featuring a continuous energy spectrum with an end point energy $E_{max}$ of 0.545 MeV, and can penetrate metals to mean implantation depths ranging from approximately 10 to 160 μm.[32]

Such a mean implantation depth, $z$, depends on material's density $\rho$ as $z[\mathrm{cm}] = \frac{E_{max}{}^{1.4}[\mathrm{MeV}]}{16 \times \rho[\mathrm{g\ cm^{-3}}]}$,[36] therefore $z$ in $GdVO_4$ of $\rho \approx 5.3$ g cm$^{-3}$ is *ca.* 50 μm. PALS probes defects in solids by exploiting the sensitivity of positron–electron annihilation to the local electronic environment. Upon implantation into the material, positrons rapidly thermalize within a few picoseconds and diffuse through the lattice.[37] In their thermalized state, positrons (as positively charged anti particles) are preferentially attracted to neutral and negatively charged open-volume defects – such as vacancies, dislocations, or voids – where the

Table 1 Structural and optical effects of various optically inactive co-dopants in $GdVO_4$:$Yb^{3+}$/$Er^{3+}$ microcrystals. $Zn^{2+}$ and $Sc^{3+}$ results originate from previous work,[19] while the effects of $Cd^{2+}$, $Bi^{3+}$, and $In^{3+}$ were studied in the present work

| Ion | Intermediate | Ion radius (pm) | Melting point (°C) | Main effect | Source |
|---|---|---|---|---|---|
| $Zn^{2+}$ | $Zn_2V_2O_7$ | 90 | 880[19] | Lattice shrinkage + structural defects + particle growth ($\sim$60$\times$ UC) | Previous work[19] |
| $Sc^{3+}$ | $ScVO_4$ | 83 | 1663[19] | Lattice shrinkage only ($\sim$20$\times$ UC) | Previous work[19] |
| $Bi^{3+}$ | $BiVO_4$ | 117 | 943[33] | Lattice expansion + moderate flux effect | Current work |
| $Cd^{2+}$ | $Cd_4Na(VO_4)_3$ | 110 | 892[34] | Particle growth + defect formation | Current work |
| $In^{3+}$ | $InVO_4$ | 92 | 1134[35] | Lattice shrinkage + charge compensation + mild flux effect | Current work |

 

Coulomb repulsion from atomic nuclei is minimized and electron density is locally reduced. Once trapped in such sites, positrons ultimately annihilate with electrons, emitting typically two 511 keV gamma photons. Importantly, the positron lifetime prior to annihilation is governed by the local electron density: lower densities (*e.g.*, in larger open defects) yield longer lifetimes, while denser regions (such as the defect-free bulk) lead to rapid annihilation.[32,37,38] Moreover, the relative intensity of different lifetime components – obtained through spectral decomposition – offers insight into the abundance of each defect type.[38,39] While this section introduces the foundational physics behind PALS, the detailed interpretation of lifetime components and their correlation to defect size, type, and concentration – along with the theoretical models used for analysis – is provided in the Results section. This structure ensures a smoother narrative flow and avoids redundancy, allowing for deeper engagement. The PALS technique can serve as a valuable complement to other bulk-sensitive characterization methods, such as electron spin resonance (ESR) spectroscopy. However, to the best of our knowledge, ESR characterization of even pure $GdVO_4$ has not been reported, likely due to the extremely broad and low-information signals originating from its magnetically dense $Gd^{3+}$ lattice. In ESR studies, isolated paramagnetic centers are typically preferred,[40,41] which makes it challenging to detect defect-related states—such as oxygen vacancies—against the strong $Gd^{3+}$ background.

Previous investigations have highlighted the utility of positron annihilation in probing defect structures relevant to luminescence. For example, in $\gamma$-$Al_2O_3$:$Mn^{4+}$,$Mg^{2+}$ nanowires, PALS, alongside XRD and photoluminescence (PL), was used to identify oxygen vacancy-rich clusters and voids that enhanced PL intensities at optimal dopant concentrations.[42] In another study on $Nd^{3+}$-doped $Y_2Si_2O_7$ phosphors, PALS was applied to analyze multiple lifetime components, which were related to structural defects within grains and at grain boundaries, affecting phase stability and emission characteristics.[43] Furthermore, in $Er^{3+}$-doped $PbO–B_2O_3–SeO_2$ glass ceramics, a correlation was drawn between increased free-volume defect concentrations – quantified *via* PALS – and the improvement in PL efficiency.[44] While these works underscore the relevance of PALS in luminescent materials, they typically focus on qualitative or partial defect–property relationships, often lacking a comprehensive, quantitative framework that integrates defect structure with phase analysis (XRD) and absolute luminescence efficiency (PLQY).

In this context, our study presents an integrated investigation aimed at quantitatively deconvoluting the structural and optical effects of co-doping in lanthanide-doped $GdVO_4$ UC phosphors. While dopant valence and ionic radius are known to influence defect formation, our work focuses on how defect spatial arrangement, clustering, and size influence upconversion efficiency. By combining PALS, XRD, and PLQY measurements, we aim to establish quantitative structure–defect–property relationships, providing a framework for rational defect engineering in co-doped $GdVO_4$. Our current investigation proceeds in two stages:

- First, we analyze the individual structural effects induced by dopants. $Zn^{2+}$ and $Cd^{2+}$, which introduce a charge imbalance, are expected to create a number of vacancy-type defects. These are directly characterized by PALS to quantify defect types. In contrast, $Sc^{3+}$ – with a smaller ionic radius and isovalent substitution – is used as a control to assess lattice contraction in the absence of charge-induced defect formation. This dopant is also examined by PALS. Additionally, XRD is also used to assess the structural impact upon co-doping.
- Second, to probe dopants that do not significantly introduce structural defects, we employ $Bi^{3+}$ and $In^{3+}$. These ions influence the lattice primarily through expansion ($Bi^{3+}$) or mild contraction ($In^{3+}$) and may act as fluxing agents during synthesis. Structural signatures are explored *via* XRD.

In each case, the corresponding optical performance is evaluated by PLQY measurements to isolate the influence of crystallographic distortion on UC efficiency. Additionally, scanning electron microscopic (SEM) images have been recorded to examine the particle size and morphology after co-doping. Together, this approach enables a systematic deconvolution of the overlapping effects of lattice modification, defect formation, and particle growth, thus offering a comprehensive understanding of the mechanisms governing UC enhancement in lanthanide-doped $GdVO_4$.

## 2. Experimental details

### 2.1. Synthesis

To synthesize the doped $GdVO_4$-based compounds, a variety of high-purity reagents were employed. $Gd(NO_3)_3·6H_2O$ ($\geq$99.9%), $Er(NO_3)_3·6H_2O$ ($\geq$99.9%), $Yb(NO_3)_3·6H_2O$ ($\geq$99.9%), $ScCl_3·6H_2O$ ($\geq$99.9%), $Zn(NO_3)_2·6H_2O$ ($\geq$99%), $CdCl_2$ ($\geq$99.9%), $Bi(NO_3)_3·5H_2O$ (99.99%), $In(NO_3)_3·xH_2O$ (99.99%) and polyvinylpyrrolidone (PVP; $M_w$ 40 000) were obtained from Sigma-Aldrich and used without further purification. The vanadium precursors, $Na_3VO_4$ and $NH_4VO_3$ (each $\geq$99% purity), were purchased from Acros Organics and used without modification.

A schematic representation of the synthesis steps is shown in Fig. 1. The standard co-precipitation procedure involved dissolving sodium vanadate (4 mM) in water to form solution A. Separately, the remaining metal salts and PVP were dissolved in an equivalent volume of water, creating solution B. Once both solutions were fully dissolved, solution A was gradually introduced into solution B under continuous stirring. Initially, the mixture remained clear but soon became turbid, eventually leading to the formation of a white precipitate within a few minutes. The amount of each component in the reaction mixture was calculated to provide nominal doping composition of $Yb^{3+}$-10%,$Er^{3+}$-2% (in all samples) and variable concentrations (5 and 15%) of co-dopants: $Sc^{3+}$, $Bi^{3+}$, $In^{3+}$, $Zn^{2+}$, and $Cd^{2+}$. $GdVO_4$:Yb/Er/$x$Me, where $x$ = 5 or 15 and Me = Sc, Bi, In, Zn, or Cd, will be further used through the paper as a name of samples. The choice of 5% and 15% co-doping concentrations is based on our previous work investigating co-doping with $Sc^{3+}$ and $Zn^{2+}$. It was demonstrated that selected 5% and 15% are

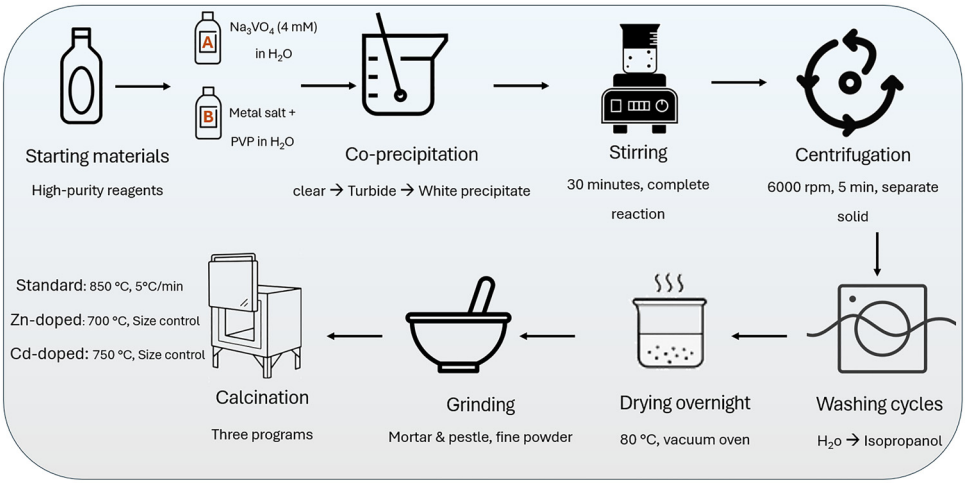


Fig. 1 Flowchart illustrating the synthesis process of doped $GdVO_4$-based compounds *via* the co-precipitation method, followed by drying and calcination.

representative concentrations—corresponding to the rising and near-maximum regions of PLQY – allowing direct comparison and focused analysis of co-dopant-induced defect interactions.[19] Hence, the selected concentrations ensure continuity with our previous dataset and effectively capture the most relevant regimes for understanding the influence of co-doping on luminescence and defect behavior.

The reaction mixture was stirred for an additional 30 min to ensure completion. Subsequently, stirring was halted, allowing the precipitate to settle naturally. The solid was then separated by centrifugation (6000 rpm for 5 minutes) and thoroughly washed multiple times with deionized water to eliminate any residual reagents. A final wash with isopropanol was performed to aid in moisture removal. The collected precipitate was dried overnight at 80 °C in a vacuum oven at 10 mbar. After drying, the material was finely ground using a mortar and pestle, then subjected to calcination at different temperatures in a muffle furnace (Thermoconcept, KLS-05/13) at 850 °C, with a ramp rate of 5 °C per minute. To mitigate the pronounced particle growth induced by $Zn^{2+}$ and $Cd^{2+}$ at 850 °C, $GdVO_4$:Yb/Er/Zn and $GdVO_4$:Yb/Er/Cd were instead calcined at 700 °C and 750 °C, respectively. The resulting calcined powder was ground once more and stored in polystyrene cuvettes for further characterization presents a flowchart summarizing the synthesis process.

### 2.2. Structural characterization

Crystal structure analysis and phase identification were performed using an X-ray powder diffractometer (Bruker D2 Phaser) equipped with Cu Kα radiation ($\lambda$ = 1.5405 Å). Data were collected with a scanning rate of 1 s per step, a 0.02° increment, and a $2\theta$ range of 10° to 80°, using a 0.1 mm slit. Rietveld refinements were conducted using TOPAS software (Bruker), and crystal structures were visualized with VESTA. The crystallite size ($D$) and microstrain ($\varepsilon$) were estimated using the Halder–Wagner–Langford equation (further details provided in the SI), with fixed values of $k$ = 0.8 and $\lambda$ = 0.15406 nm. Peak broadening at half-maximum intensity ($\beta$) was determined by fitting diffraction peaks with a pseudo-Voigt function using Origin software, as detailed in the SI. Elemental composition of the calcined phosphors was analyzed using X-ray fluorescence (XRF) spectroscopy on a Bruker S8 TIGER wavelength-dispersive spectrometer. Data acquisition and processing were carried out with the Quant-Express software (Bruker AXS), a pre-calibrated, standardless program supplied with the instrument, capable of analyzing approximately 70 elements ranging from fluorine to uranium.[45]

The microstructure of the calcined powders was imaged using a scanning electron microscope (SEM; Zeiss Supra 60VP) equipped with an SE-II detector. The samples were sputter coated with a thin layer of silver (~10 nm) to aid the SEM imaging.

### 2.3. Optical properties

The calcined powders were placed in polystyrene cuvettes and compacted by repeated tapping. These samples were excited using 980 nm continuous-wave (CW) laser diode (Thorlabs, L980P200). The PLQY measurements were performed using a custom-built optical setup[29] based around an integrating sphere (Labsphere, Ø15 cm, 3P-LPM-060-SL) and a CCD spectrometer (Avantes, AvaSpec-ULS2048 × 64TEC). The setup was calibrated using a calibration lamp (Ocean Optics, HL-3plus-INT-CAL-EXT). The relative error for PLQY measurement for repeatedly synthesized samples was found to be ±5%. This was attributed to the variation in degree of powder compaction within the cuvettes leading to diffuse reflectance and reabsorption of light, thereby resulting in variation of the calculated PLQY values. Despite several attempts to improve the repeatability of the packing density of powders within the cuvettes, this variability remained a source of measurement uncertainty. Future work could focus on developing standardized compression methods to achieve more consistent powder packing, which would enhance the reliability and reproducibility of diffuse reflectance measurements.

 

### 2.4. PALS setup

PALS measurements involved a digitizer (Acqiris DC 282, 10-bit vertical resolution) and three photomultiplier tubes (PMTs) with $Ce_2Br_3$ scintillators provided by Scionix Holland. Two scintillators were $\varnothing$ = 51 mm and $h$ = 10 mm, while the third was $\varnothing$ = 51 mm and $h$ = 25.4 mm, strategically positioned to optimize spatial coverage and minimize backscattered photon detection. A custom data acquisition software[46] facilitated simultaneous signal detection, enabling six positron lifetime spectra collection in one session, reducing measurement time accordingly. The sample holder, designed for $\sim$300 mm$^3$ of powdered sample, housed a 20 μCi $^{22}$Na positron source sealed within 5 μm Kapton® foil (DuPont de Nemours™). A PALS spectrum is described by $N(t) = \sum \left[\frac{1}{\tau_i} I_i e^{\frac{-t}{\tau_i}}\right]$, with $\tau_i$ and $I_i$ ($\sum I_i = 1$) are the positron lifetime and intensity of the $i$th component, respectively.[38,47] Hence, PALS analysis comprised fitting exponential decay curves to histograms of recorded time differences. Al and Sn reference samples with known lifetimes were used to estimate the resolution functions and source contribution. About 10.60% of all positrons annihilate within the used source itself, and therefore this value is referred as source contribution (shared between Kapton foil (0.382 ns/10.40%) and glue (2.60 ns/0.20%)) and an average time resolution of 0.28 ns (at full width at half maximum) have been defined during the fitting process.

## 3. Results

### 3.1. Structural analysis

Fig. 2 shows the XRD patterns of undoped and co-doped $GdVO_4$ samples. All patterns correspond to $GdVO_4$ crystals with the Zircon structure and crystallized in the tetragonal $I4_1/amd$ space group. In order to further investigate the effect of co-doping, we performed Rietveld refinement of the XRD spectra to obtain information on phase purity and cell parameters (the quality of the refinement is shown in Fig. 2, while the quantitative results are summarized in Table 2). Co-doping with standard concentrations – hereinafter the concentrations represent percentage of $Gd^{3+}$ ions substituted by $Yb^{3+}$, $Er^{3+}$, and other dopants – of $Yb^{3+}$ (10 mol%) and $Er^{3+}$ (2 mol%) doesn't change the phase but leads to a reduction of the cell volume (and the crystallographic parameters $a$, $b$ and $c$). This is expected as the ionic radii of $Er^{3+}$ (100 pm) and $Yb^{3+}$ (99 pm) are smaller than that of $Gd^{3+}$ (105 pm). Simultaneously, co-doping with $Er^{3+}$ and $Yb^{3+}$ leads to decrease of crystallite size to 29 ± 1 nm *vs.* 44 ± 2 nm (for the undoped sample) and increase of strain to (6.3 ± 1.1) × $10^{-3}$ from (3.3 ± 1.3) × $10^{-3}$, respectively.

The calculations of crystallite size and strain were performed using Williamson–Hall–Langford (WHL) method (Fig. S1–S12, SI). It is known from the literature that using different equations, such as Williamson–Hall, Halder–Wagner, or size-strain plot[48] results in slightly different values of crystallite size and

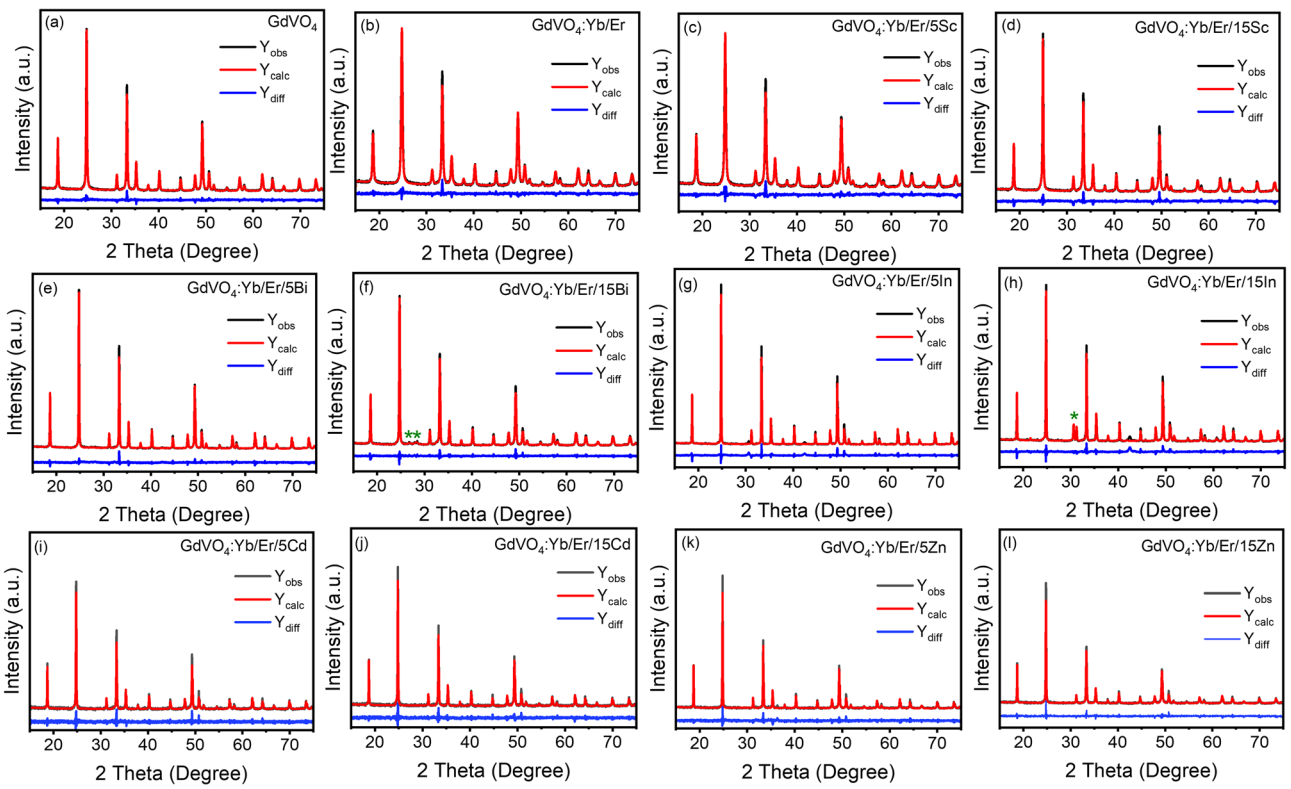


Fig. 2 XRD spectra ($Y_{obs}$), result of Rietveld refinement ($Y_{calc}$) and difference between $Y_{obs}$ and $Y_{calc}$ ($Y_{diff}$) of samples with different nominal doping compositions. Always 10% and 2% for $Yb^{3+}$ and $Er^{3+}$, respectively and 5% (c), (e), (g), (i) and (k) and 15% (d), (f), (h), (j) and (l) of ions such as $Sc^{3+}$ (c) and (d), $Bi^{3+}$ (e) and (f), $In^{3+}$ (g) and (h), $Cd^{2+}$ (i) and (j), and $Zn^{2+}$ (k) and (l).

microstrain. Taking this potential source of error into account, we use these values primarily as an indicator for trends in the in the variation of crystallite size and micro-strain with co-doping.

The addition of $Sc^{3+}$ with an ionic radius of 87 pm leads to a decrease in the cell volume and crystallographic parameters (compared to $GdVO_4$:Yb/Er) (Table 2). This observation is valid for both nominal $Sc^{3+}$ concentrations (5 and 15 mol%) and the reduction in cell volume is greater at the higher concentration of $Sc^{3+}$. To confirm the presence of $Sc^{3+}$ in the co-precipitated sample, the elemental composition was analyzed using XRF – a non-destructive method that detects characteristic X-rays emitted by elements upon excitation with high-energy X-rays. This technique allowed quantification of the relative amounts of $Gd^{3+}$, $Yb^{3+}$, $Er^{3+}$, and $Sc^{3+}$. Under the assumption that $Yb^{3+}$, $Er^{3+}$ and $Sc^{3+}$ substitute $Gd^{3+}$, the compositions of $(Gd_{0.79}Yb_{0.13}Er_{0.02}Sc_{0.06})VO_4$ and $(Gd_{0.72}Yb_{0.12}Er_{0.03}Sc_{0.13})VO_4$ were found with nominal $Sc^{3+}$ concentration of 5 and 15%, respectively. The only small deviations between nominal and experimental concentrations indicate successful co-doping with $Sc^{3+}$ ions *via* co-precipitation method. Microstructural analysis of XRD data using the WHL method results in crystallite size of 30 ± 1 nm (for 5% $Sc^{3+}$) and 51 ± 4 nm (for 15% $Sc^{3+}$) and micro-strain of (7.5 ± 0.9) × $10^{-3}$ and (7.0 ± 0.8) × $10^{-3}$, respectively (Fig. 3 and Fig. S13).

Co-doping with nominal 5 mol% $Bi^{3+}$ (ionic radius – 117 pm) results in pure $GdVO_4$ phase. In contrast, 15% $Bi^{3+}$ provides an additional phase – 5.3 wt% identified as $Bi_{23}(VO_4)_4O_{28.5}$ based on the powder diffraction file PDF 04-020-1954 (Fig. 2f). The substantial increase in cell volume was only observed at 15% nominal $Bi^{3+}$ doping (Table 2). In order to understand exactly how much $Bi^{3+}$ is present in the samples, an XRF analysis was carried out, similar to the $Sc^{3+}$ doped samples. The compositions $(Gd_{0.79}Yb_{0.12}Er_{0.02}Bi_{0.06})VO_4$ and $(Gd_{0.68}Yb_{0.12}Er_{0.02}Bi_{0.18})VO_4$ were found for the samples with nominal $Bi^{3+}$ concentrations of 5 and 15% respectively. The amount of $Bi^{3+}$ found is slightly larger than expected from the nominal composition with 15% co-doping, which can be explained by the existence of a secondary Bi-based phase $Bi_{23}(VO_4)_4O_{28.5}$. Microstructural analysis of XRD data using the WHL method shows an increase in crystallite size, 80 ± 10 nm (for 5% $Bi^{3+}$) and 46 ± 9 nm (for 15% $Bi^{3+}$) compared to the $GdVO_4$:Yb/Er sample. Similarly, compared to the $GdVO_4$:Yb/Er sample, the microstrain decreases in the sample with 5% $Bi^{3+}$ – (1.9 ± 1.7) × $10^{-3}$ (Fig. S13). In contrast, the reduction is less pronounced in the sample with 15% $Bi^{3+}$, where the microstrain reaches – (4.0 ± 2.4) × $10^{-3}$ (Fig. 3).

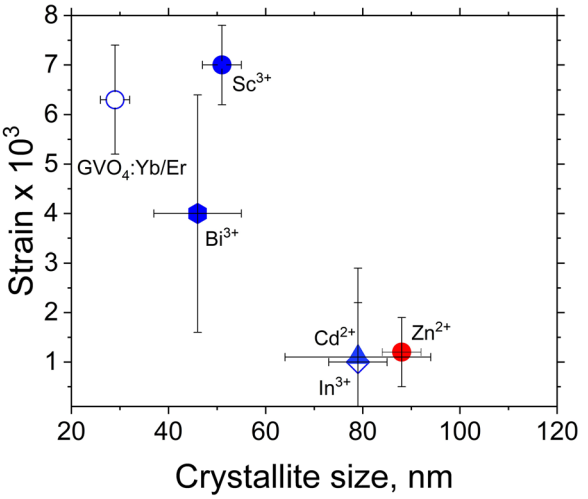


Fig. 3 Summary of crystallite size and microstrain calculated using WHL equation for samples with 15% of $Sc^{3+}$, $Bi^{3+}$, $In^{3+}$, $Zn^{2+}$, $Cd^{2+}$ and the reference $GVO_4$:Yb/Er sample.

As the ionic radius of $In^{3+}$ (92 pm) is smaller than the lanthanide ions ($Gd^{3+}$, $Yb^{3+}$, $Er^{3+}$), the co-doping with $In^{3+}$ leads to a decrease of the crystallographic parameters (Table 2). This effect can be observed for both nominal doping concentrations. Furthermore, the use of nominal concentration of 15% leads to appearance of a secondary phase – $In_2O_3$ (8.6 wt%) (Fig. 2h). The compositions of $(Gd_{0.80}Yb_{0.12}Er_{0.02}In_{0.06})VO_4$ and $(Gd_{0.67}Yb_{0.11}Er_{0.02}In_{0.20})VO_4$ were found for the samples with nominal $Bi^{3+}$ concentration 5 and 15%, respectively. The apparent increase in $In^{3+}$ content beyond the nominal 15% is likely attributable to the formation of the secondary $In_2O_3$ phase. Co-doping with 5% mol% $In^{3+}$ still provides pure $GdVO_4$ phase, and the experimental composition is close to the nominal one. Microstructural analysis of XRD data using the WHL method results in increased crystallite size of 111 ± 14 nm, (for 5% $In^{3+}$) and 79 ± 15 nm (for 15% $In^{3+}$). Simultaneously, the microstrain was calculated as (2.0 ± 1.2) × $10^{-3}$ and (1.1 ± 1.0) × $10^{-3}$, respectively (Fig. 3 and Fig. S13).

As the next ion to be compared, $Cd^{2+}$ co-doping was investigated. Ionic radius of $Cd^{2+}$ (110 pm) is significantly larger than radius of lanthanides. Table 2 indicates that co-doping with $Cd^{2+}$ (the sample was calcined at lower temperature of 750 °C to maintain the particle size compared to co-doping with other ions) leads to a pronounce increase of cell volume. However, the analysis of chemical composition shows some deficiency of $Cd^{2+}$ in comparison to the nominal composition – $(Gd_{0.84}Yb_{0.13}Er_{0.02}Cd_{0.01})VO_4$ (for 5% $Cd^{2+}$) and $(Gd_{0.80}Yb_{0.14}Er_{0.02}Cd_{0.04})VO_4$ (for $Cd^{2+}$). The crystallite size increases up to 80 ± 5 nm and 79 ± 6 nm for co-doping with 5 and 15% $Cd^{2+}$, respectively. The microstrain decreases with amount of

Table 2 Crystallographic parameters of $GdVO_4$ and metal ion $GdVO_4$:Yb/Er co-doped phosphorous

| Sample | $a = b$ (pm) | $c$ (pm) | $V$ (pm$^3$) × $10^6$ | Goodness of FIT |
|---|---|---|---|---|
| $GdVO_4$ | 721.18 | 635.16 | 330.35 | 1.32 |
| $GdVO_4$:Yb/Er | 719.97 | 634.41 | 328.85 | 1.41 |
| $GdVO_4$:Yb/Er/5Sc | 718.86 | 633.95 | 327.60 | 1.50 |
| $GdVO_4$:Yb/Er/15Sc | 715.61 | 632.39 | 323.84 | 1.57 |
| $GdVO_4$:Yb/Er/5Bi | 719.37 | 634.75 | 328.48 | 1.59 |
| $GdVO_4$:Yb/Er/15Bi | 720.02 | 635.84 | 329.65 | 1.46 |
| $GdVO_4$:Yb/Er/5In | 718.86 | 633.94 | 327.59 | 2.02 |
| $GdVO_4$:Yb/Er/15In | 717.64 | 633.77 | 326.40 | 1.96 |
| $GdVO_4$:Yb/Er/5Cd | 719.22 | 633.64 | 327.77 | 1.10 |
| $GdVO_4$:Yb/Er/15Cd | 719.58 | 633.96 | 328.26 | 1.11 |
| $GdVO_4$:Yb/Er/5Zn | 719.08 | 633.52 | 327.58 | 1.12 |
| $GdVO_4$:Yb/Er/15Zn | 718.97 | 633.51 | 327.47 | 1.20 |

$Cd^{2+}$ – $(1.7 \pm 0.8) \times 10^{-3}$ and $(1.0 \pm 1.9) \times 10^{-3}$ for 5% and 15% $Cd^{2+}$, respectively (Fig. 3 and Fig. S13).

Co-doping with $Zn^{2+}$ leads to a reduction in the lattice parameters and overall unit cell volume (Table 2) of $GdVO_4$:Yb/Er, consistent with the substitution of smaller $Zn^{2+}$ ions (ionic radius 90 pm) for the larger $Gd^{3+}$ ions (105 pm). The composition of the synthesized materials, $(Gd_{0.78}Yb_{0.12}Er_{0.02}Zn_{0.08})VO_4$ and $(Gd_{0.62}Yb_{0.11}Er_{0.02}Zn_{0.25})VO_4$, confirms successful incorporation of $Zn^{2+}$ into the lattice. Interestingly, while the unit cell contracts due to the smaller ionic radius of $Zn^{2+}$, the crystallite size increases, reaching $76 \pm 8$ nm and $88 \pm 4$ nm for 5% and 15% $Zn^{2+}$ co-doping, respectively. This size growth is accompanied by a reduction in microstrain, from the baseline value to $(3.2 \pm 1.0) \times 10^{-3}$ (for 5% $Zn^{2+}$) and $(1.2 \pm 0.7) \times 10^{-3}$ (for 15% $Zn^{2+}$). These trends suggest improved crystalline order and fewer structural imperfections upon $Zn^{2+}$ incorporation (Fig. 3 and Fig. S13). It should be noted that an increase in crystallite size and a decrease in macrostrain were observed despite the lower calcination temperature of 700 °C in contrast to 850 °C (for $Sc^{3+}$, $Bi^{3+}$ and $In^{3+}$) to maintain the particle size.

The microstructural information obtained from XRD analysis is further corroborated by SEM observations. It is important to note that different calcination temperatures were applied for the $Zn^{2+}$ and $Cd^{2+}$ co-doped samples in order to achieve comparable particle size, ensuring a meaningful comparison between their morphological and structural characteristics. Previous findings demonstrated that calcination of $Zn^{2+}$ co-doped samples at 850 °C results in the formation of large particles, typically on the order of ~1000 nm.[19]

SEM images reveal that the samples $GdVO_4$, $GdVO_4$:Yb/Er, $GdVO_4$:Yb/Er/5Sc, $GdVO_4$:Yb/Er/15Sc, and $GdVO_4$:Yb/Er/5Cd (Fig. 4a–d and i, respectively) exhibit similar particle size. The powder consists of partially sintered small nanoparticles (~70 nm scale) that cluster together to form loosely packed agglomerates on the micron size scale. It appears that even small amount (5%) of $Bi^{3+}$ facilitated crystallization of $GdVO_4$ (Fig. 4e) resulting in formation of particles exhibiting a mix of rod-like structures (100–300 nm range in length) and aggregated clusters with relatively rough surface. Increase concentration of $Bi^{3+}$ doesn't change particles view (Fig. 4f). Doping with $In^{3+}$ (Fig. 4g and k) results in particles (with size 400–600 nm) exhibiting a smooth, faceted, and polyhedral morphology. Some small nanoscale deposits or secondary formations can be observed on the surface, which might be the secondary phase of $In_2O_3$. When $GdVO_4$ is doped with of $Cd^{2+}$ and $Zn^{2+}$ ($GdVO_4$:Yb/Er/15Cd and $GdVO_4$:Yb/Er/5Zn samples, Fig. 4j and k, respectively), the micrographs reveal a densely packed morphology composed of aggregated, rounded nanoparticles that have grown in size to reach a scale of up to ~300 nm. The particles formed in the presence of 15% $Zn^{2+}$ (Fig. 4l) resemble those observed in case of $In^{3+}$ co-doping (Fig. 4h), despite the lower calcination temperature of 700 °C *vs.* 850 °C, respectively.

### 3.2. Optical properties

The UC spectra of synthesized samples are defined by the electronic levels of the lanthanide ions used for co-doping, namely $Yb^{3+}$ and $Er^{3+}$. The $Yb^{3+}$ has only one excited electronic state $^2F_{5/2}$ which can be populated from the ground state $^2F_{7/2}$ using a 980 nm laser. The $^2F_{5/2}$ state of $Yb^{3+}$ is in resonance

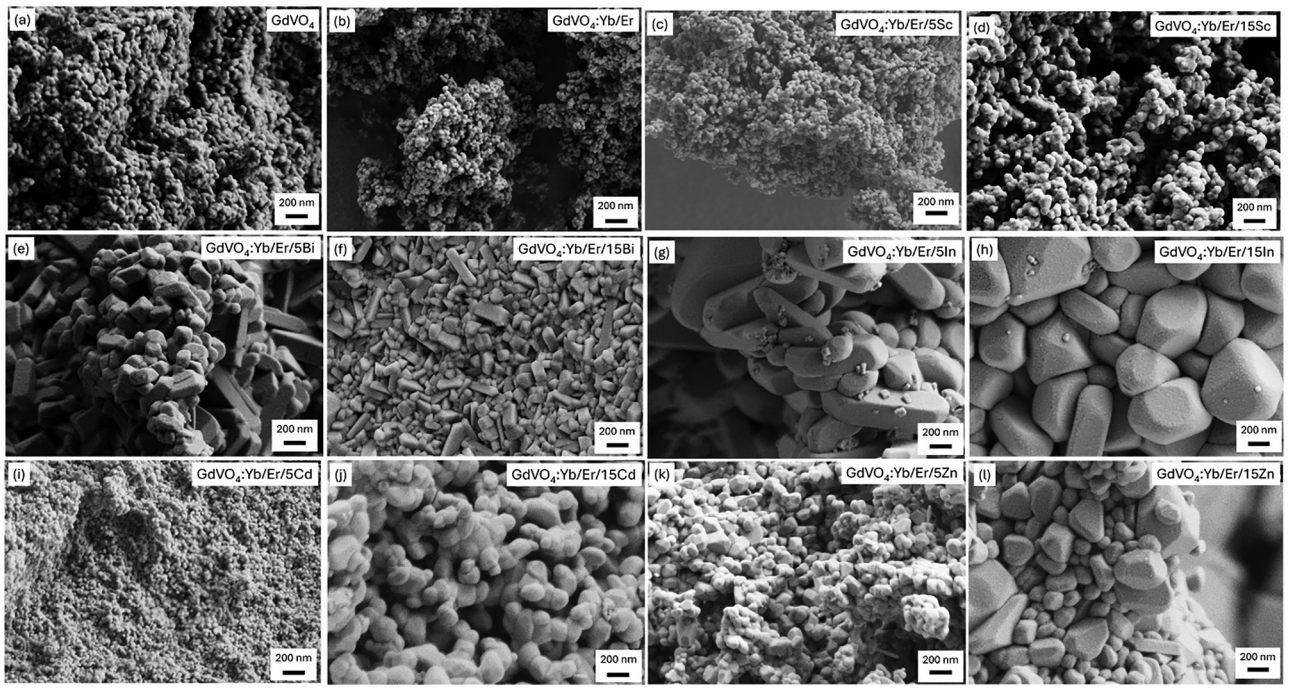


Fig. 4 Summary of SEM images of samples with different nominal doping compositions. Always 10% and 2% for $Yb^{3+}$ and $Er^{3+}$, respectively and 5% (c), (e), (g), (i) and (k) and 15% (d), (f), (h), (j) and (l) of ions such as $Sc^{3+}$ (c) and (d), $Bi^{3+}$ (e) and (f), $In^{3+}$ (g) and (h), $Cd^{2+}$ (i) and (j), and $Zn^{2+}$ (k) and (l).

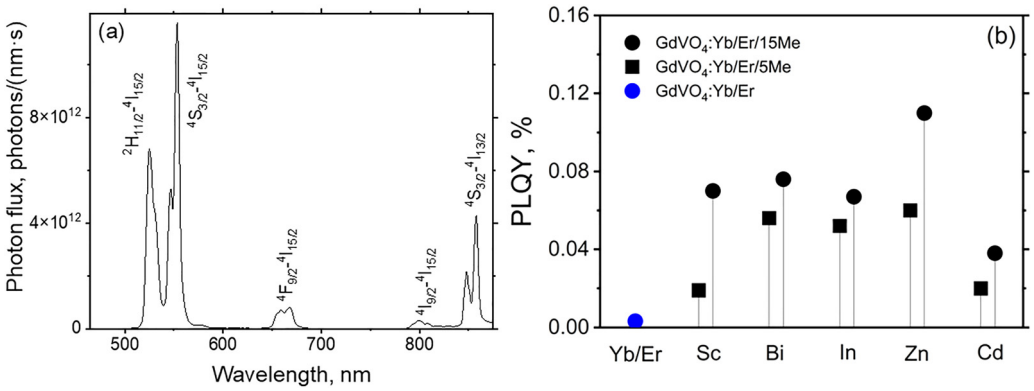


Fig. 5 (a) UC luminescence of $GdVO_4$:Yb/Er/15Bi sample excited with 980 nm laser with intensity of 15 W $cm^{-2}$; (b) PLQY of $GdVO_4$:Yb/Er samples co-doped with 5 and 15% $Sc^{3+}$, $Bi^{3+}$, $In^{3+}$, $Zn^{2+}$ and $Cd^{2+}$.

with the $^4I_{11/2}$ state of $Er^{3+}$, allowing efficient energy transfer from $Yb^{3+}$ to $Er^{3+}$. As the $^4I_{11/2}$ state is long-lived (with a lifetime of several milliseconds), it can participate in the energy transfer UC by interacting with a second $^4I_{11/2}$ state, giving rise to the high-energy $^2H_{9/2}$ state. The latter undergoes rapid non-radiative relaxation to the $^4F_{7/2}$ state. The $^4F_{7/2}$ state is a key state for the appearance of multiband UC luminescence of $Er^{3+}$ in the visible and near-infrared region (Fig. 5a), where the exact balance between the intensity of the luminescence peaks is defined by the crystal structure, the maximum phonon energy and the concentration of lanthanide ions. Since additional co-doping ions ($Sc^{3+}$, $Bi^{3+}$, $In^{3+}$, $Cd^{2+}$ and $Zn^{2+}$) do not have electronic levels that potentially interact with electronic levels of $Yb^{3+}$ and $Er^{3+}$ in the vis/NIR region, the position of luminescence peaks in the UC spectra of the $GdVO_4$:$Yb^{3+}$/$Er^{3+}$ sample remain unchanged and only their intensity varies depending on which ion ($Sc^{3+}$, $Bi^{3+}$, $In^{3+}$, $Cd^{2+}$ or $Zn^{2+}$) is used as co-dopand. Fig. 5a shows representative UC spectra of $GdVO_4$:Yb/Er/5Bi samples, whereas UC spectra with other co-dopants are presented in SI (Fig. S14–S18). Fig. 5a shows that 980 nm excitation results in dominant visible emission from the $^4F_{7/2}$, $^2S_{3/2}$ states (visually the emission is detected as green light from the excitation spot), while the other prominent peak from the $^2F_{9/2}$ peak to the ground state is weak. A similar observation can be seen in Fig. S14–S18.

Steady-state luminescence spectra were excluded from comparative analysis because of the unpredictable and sample-dependent influence of light scattering, which may distort intensity readings. Instead, we measured the absolute UC PLQY using an integrating sphere. PLQY, defined as the ratio of emitted to absorbed photons, serves as a key figure-of-merit for luminescence, enabling a quantitative comparison of different materials. Fig. 5b summarizes the UC PLQY values of $GdVO_4$:Yb/Er UC materials synthesized in the presence of a series of additional ions ($Sc^{3+}$, $Bi^{3+}$, $In^{3+}$, $Cd^{2+}$ and $Zn^{2+}$). All measurements of UC PLQY were performed at excitation intensity of 15 W $cm^{-2}$. It is important to note that the goal is not to obtain the most efficient UC material, but rather to elucidate the role of co-dopants using PLQY as a figure-of-merit parameter. The reference material, with a UC PLQY of 0.003%, is a $GdVO_4$:Yb/Er sample synthesized *via* co-precipitation followed by calcination at 850 °C. While the UC PLQY value is low, it can still be measured with high precision. The uncertainty in UC PLQY measurements depends mainly on the percentage of absorbed light and the uncertainty in our experiments is relatively low (<10%) as all samples absorb 30–40% of the incident radiation.[49] Fig. 5b shows that co-doping with $Sc^{3+}$ enhances UC PLQY, reaching 0.02% and 0.07% for 5% and 15% $Sc^{3+}$, respectively. These results are consistent with previously reported values,[19] highlighting the reproducibility of both the synthesis approach and the optical characterization methodology. Co-doping with $Bi^{3+}$ and $In^{3+}$ also improves PLQY at lower doping concentrations (5%) – achieving 0.06 and 0.05%, respectively; however, at 15% doping, the PLQY remains comparable to that of $Sc^{3+}$ co-doping – achieving 0.08 and 0.07%, respectively. Co-doping with $Cd^{2+}$ gives a slightly lower PLQY of 0.02 and 0.04% for 5 and 15% $Cd^{2+}$ respectively. Notably, the most significant increase in PLQY was observed with $Zn^{2+}$ co-doping, achieving PLQY of 0.06 and 0.11% for 5 and 15% $Zn^{2+}$, respectively. This represents a 37-fold increase over the reference sample and a 1.4-fold increase over the second-best co-dopant – $Bi^{3+}$, despite the much lower calcination temperature of 700 °C used for $Zn^{2+}$-containing samples.

### 3.3. Positron annihilation spectroscopy

To elucidate the evolution of defect microstructure in $GdVO_4$ upon metal ion doping, we performed PALS measurements on undoped and doped powder samples. As outlined in the introduction, positron lifetimes and their associated intensities provide insights into the size and concentration of open-volume defects, respectively. These parameters enable tracking of changes in the defect landscape induced by doping. The recorded spectra were analyzed with the PALSfit software,[50] which identified two distinct sample-related lifetime components, $\tau_1$ and $\tau_2$, along with their intensities $I_1$ and $I_2$. The simple trapping model (STM)[37,51] provides a framework for interpreting such spectra when a single defect type is predominant. Within this model, $\tau_2$ corresponds to positrons trapped and annihilated at vacancy-type defects. Conversely, $\tau_1$ is shorter than the bulk lifetime, $\tau_{bulk}$. This reduced bulk lifetime

 

$\tau_1$ arises from the combined effects of positron trapping and detrapping dynamics, which modulate annihilation rates in the bulk or near-bulk states.[32] The intensities relate to the fraction of positrons annihilating in these states, with $I_1 = 1 - I_2$ assuming a single trapping site. Using the STM, the bulk lifetime $\tau_{bulk}$ can be reconstructed from the lifetime components as:

$$\frac{1}{\tau_{bulk}} = \frac{I_1}{\tau_1} + \frac{I_2}{\tau_2} \quad (1)$$

Discrepancies from this expression indicate the presence of complex trapping scenarios involving multiple defect types or shallow traps, which cannot be fully resolved in the two-component lifetime analysis. The average positron lifetime, calculated as $\tau_{avg} = \tau_1 I_1 + \tau_2 I_2$, serves as a cumulative indicator of the material's defect content. An average positron lifetime exceeding that of defect-free bulk material signifies the presence of open-volume defects,[52] and correlates with defect type and density.[53]

**3.3.1. Undoped $GdVO_4$.** In the baseline undoped state of $GdVO_4$, the experimentally resolved positron lifetime components are $\tau_1$ = 170 ps and $\tau_2$ = 348 ps (Fig. 6a). The relative intensity of the short component ($I_1$) is less than 50%, indicating that a significant fraction of positrons is trapped at open-volume defects. The longer lifetime component $\tau_2$ is therefore attributed to positrons annihilating at specific defect sites. At first glance, the value of $\tau_1$ may appear to align with the behavior expected under the STM framework, in which $\tau_1$ is interpreted as a shortened bulk lifetime due to positron trapping and detrapping dynamics. To test the validity of this assumption, we applied eqn (1) to back-calculate the effective bulk lifetime from the measured components and intensities. Surprisingly, the reconstructed $\tau_{bulk}$ value is approximately 300 ps – significantly longer than the theoretically predicted bulk positron lifetime in defect-free $GdVO_4$ (*i.e.*, the delocalized bulk state) of ~182.2 ps (Table S1) obtained from *ab initio* density functional theory (DFT) calculations using the atomic superposition (AtSup) method.[54–56] These simulations treat electron–positron interactions within the local density approximation (LDA), modeling the positron as embedded in a homogeneous electron gas. The Boronski–Nieminen (BN) scheme[54] was employed to incorporate electron–positron correlation effects and incomplete positron screening. This pronounced discrepancy between experimental reconstruction and theoretical expectation (300 ps *vs.* 182.2 ps) clearly violates the validity of the STM – that a single dominant defect species governs positron trapping in $GdVO_4$. Instead, it strongly suggests the presence of multiple, unresolved defect types contributing to the annihilation spectrum averaged in $\tau_1$. For instance, the $\tau_1$ component likely represents a superposition of positron annihilation in near-bulk regions and shallow positron traps.[57] Such shallow traps, including dislocations and strain-induced imperfections, typically feature weak binding energies (10–100 meV),[58] allowing thermal detrapping and contributing lifetimes only

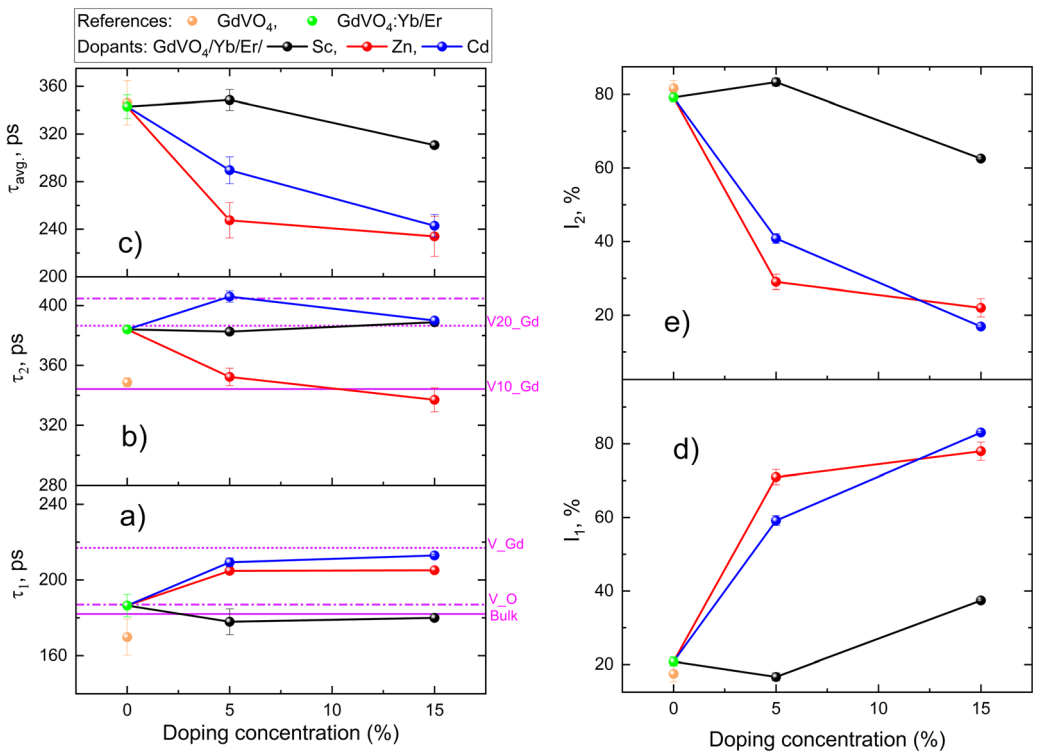


Fig. 6 Influence of $Zn^{2+}$, $Sc^{3+}$, and $Cd^{2+}$ ion doping concentrations in $GdVO_4$:$Yb^{3+}$/$Er^{3+}$ on: (a) positron lifetime in bulk, monovacancies, and dislocations-$\tau_1$, (b) positron lifetime in vacancy clusters at grain boundaries-$\tau_2$, (c) average positron lifetime, $\tau_{avg}$. (d) and (e) Are the corresponding intensities. The results of undoped $GdVO_4$ reference is shown as orange circles. The results of $GdVO_4$:$Yb^{3+}$/$Er^{3+}$ sample is shown as green circles. Magenta lines in panels (a) and (b) illustrate the AtSup results for bulk and defect-related lifetimes in doped and undoped variants.

slightly longer than the bulk. These shallow traps are often active at low temperatures and remain unresolved at room temperature.

To further investigate this hypothesis, we performed temperature-dependent PALS measurements (Fig. S19, SI). The results show a reduction in the average lifetime upon cooling – a behavior consistent with the observation of shallow traps.[38] However, the temperature-dependent changes also suggest the presence of neutral defects in addition to the shallow traps.[38] Most likely, these neutral defects are oxygen vacancies (V_O), which according to DFT calculations exhibit a lifetime of 187 ps (Table S1). The observed $\tau_1$ = 170 ps thus reflects the weighted average of reduced bulk annihilation, shallow trap contributions (dislocations), and neutral oxygen vacancy trapping. Although the presence of such defects would typically lead to a $\tau_1$ value exceeding the bulk lifetime, the reduced bulk contribution – with its intrinsically shorter lifetime and higher annihilation probability – appears to dominate. This indicates that the influence of defect-related trapping is relatively minor, and the reduced bulk state largely determines the observed $\tau_1$. Worth noting, because $\tau_1$ contains unresolved contributions from multiple defect types, absolute defect densities cannot be reliably calculated (see the PALS section in SI). This limitation applies equally to doped samples, where unresolved contributions from shallow traps and/or oxygen vacancies would similarly obscure individual defect signatures. Meanwhile, $\tau_2$ is more reliably assigned to annihilation at deeper defects. Based on DFT simulations (Table S2), $\tau_2$ corresponds to positrons trapped at big neutral clusters involving Gd atoms (*ca.* V10_Gd), as shown in Fig. 6b. Likely, these defect clusters are located at grain boundaries.

**3.3.2. $GdVO_4$:Yb/Er.** The calculated bulk lifetime by Atsup for $GdVO_4$:Yb/Er sample is 182.72 ps (solid magenta line in Fig. 6a and Table S1), representing only a slight increase of 0.5 ps above the calculated value of undoped $GdVO_4$. Experimentally, the shorter positron lifetime component, $\tau_1$, increases from 170 ps in the undoped sample to 186 ps (Fig. 6a), indicating a modified annihilation environment for positrons. As previously discussed, the $\tau_1$ component in the undoped sample likely reflects a cumulative contribution from reduced bulk annihilation, dislocations, and neutral V_O. The rise in $\tau_1$ upon doping is therefore best understood as resulting from an increased presence of both dislocations and V_O, driven by local strain introduced by the ionic size mismatch between the dopant ions ($Yb^{3+}$/$Er^{3+}$) and the host $Gd^{3+}$. This strain promotes the formation of extended defects and alters the energetics of vacancy formation.

XRD analysis (Table 1 and Fig. 3) confirms lattice contraction and increased microstrain in the $Yb^{3+}$/$Er^3$-doped samples, consistent with dopant-induced structural distortion. While dislocations may be still present, their limited trapping efficiency at room temperature renders their contribution to $\tau_1$ relatively minor. More importantly, the observed $\tau_1$ = 186 ps matches well with DFT predictions for neutral V_O (Table S1), indicating their enhanced formation. Despite the isovalent nature of $Yb^{3+}$/$Er^{3+}$, their size mismatch perturbs the bonding network, facilitating V_O generation. Temperature-dependent PALS (Fig. S19) further supports this interpretation: the change is less pronounced than in the undoped reference. In the doped state, this weaker temperature dependence of $\tau_{avg}$ (constant values until 100 K) implies a shift in the dominant trapping mechanism. Specifically, it suggests that positron annihilation predominantly occurs in neutral defects, V_O, which remain effective across the temperature range. The increasing abundance of V_O in the $Yb^{3+}$/$Er^{3+}$ doped material thus tends to stabilize $\tau_{avg}$ closer to its room temperature value, effectively masking the temperature sensitivity typically associated with shallower traps.

Simultaneously, the longer lifetime component $\tau_2$ increases from 348 ps in the undoped sample to 384 ps in the doped case (Fig. 6b). Based on DFT modeling, this value corresponds to annihilation at quite larger open-volume defects such as twenty-atom gadolinium vacancy clusters ($V_{20}$_Gd), which likely form at grain boundaries under the influence of accumulated strain.

Interestingly, the intensities $I_1$ and $I_2$ remain nearly unchanged compared to the undoped $GdVO_4$ (Fig. 6d and e), indicating that the overall positron trapping probability has not substantially increased, despite the introduction of additional defect types such as neutral V_O and large gadolinium vacancy clusters ($V_{20}$_Gd). Similarly, the average positron lifetime $\tau_{avg}$ (Fig. 6c) exhibits only minor variation upon doping. This outcome may seem unexpected, given the considerable reduction in crystallite size from 44 $\pm$ 2 nm in the undoped sample to 29 $\pm$ 1 nm in the $Yb^{3+}$/$Er^{3+}$-doped material – an effect typically associated with enhanced positron trapping at grain boundaries, which would be reflected by an increase in $I_2$. The stable value of $I_2$, however, suggests that positron trapping at bulk-related defects, effectively competes with trapping at grain boundaries. This indicates a reduced positron diffusion length, limiting the probability of positrons reaching grain boundaries before annihilation. Consequently, the effective defect density probed by $\tau_{avg}$ remains nearly constant, highlighting the dominant role of bulk trapping centers in the doped material.

**3.3.3. $GdVO_4$:Yb/Er/Sc.** Upon $Sc^{3+}$ co-doping into $GdVO_4$:Yb/Er (the reference for metal ions co-doped states), a modest decrease in $\tau_1$ at is observed (Fig. 6a) at 5% and 15% Sc concentrations, with values approaching the calculated bulk lifetime from AtSup. This reduction in $\tau_1$ is directly associated with the substitution of larger $Gd^{3+}$ ions (105 pm) by smaller $Sc^{3+}$ ions (87 pm), leading to pronounced lattice contraction, as confirmed by XRD analysis. The calculated positron lifetimes from AtSup (Table S3, SI) for these contracted lattices fall within the range of 178–180 ps, which closely matches the experimental $\tau_1$ values. This observation is also consistent with theoretical predictions that co-doping with isovalent $Sc^{3+}$ substituting for $Gd^{3+}$ does not lead to the formation of monovacancies. Moreover, the convergence of $\tau_1$ toward the bulk lifetime suggests a marked reduction, or even elimination, of neutral V_O as effective positron trapping centers. Possibly, lattice contraction in the $Sc^{3+}$ co-doped system increases the formation energy of oxygen vacancies, thereby making their

 

generation less favorable. Additionally, XRD microstrain values increase with Sc content – rising from $6.3 \pm 1.1 \times 10^{-3}$ in $GdVO_4$:Yb/Er to $7.5 \pm 0.9 \times 10^{-3}$ at 5% Sc and $7.0 \pm 0.8 \times 10^{-3}$ at 15% Sc – implying that dislocations may become more abundant. However, unlike the $GdVO_4$:Yb/Er reference state where V_O acted as strong positron traps, dislocations remain relatively inefficient in capturing positrons at room temperature. Thus, although dislocations may accumulate upon Sc doping, their impact on $\tau_1$ remains limited, and positron annihilation increasingly reflects bulk-like regions.

Notably, the vacancy cluster-related positron lifetime component, $\tau_2$, remains essentially unchanged upon $Sc^{3+}$ co-doping (Fig. 6b), indicating that the nature and size of these open-volume defects are not significantly altered. In contrast, the intensities $I_1$ and $I_2$ exhibit notable variation as a function of $Sc^{3+}$ concentration (Fig. 6d and e). This behavior can be interpreted in the context of crystallite size evolution. At 5% $Sc^{3+}$, the average crystallite size ($\sim$30 nm) permits a larger fraction of positrons to diffuse toward and annihilate at vacancy clusters located at grain boundaries, contributing to the elevated $I_2$. However, when the $Sc^{3+}$ concentration increases to 15%, the crystallite size expands to $\sim$51 nm, thereby increasing the likelihood that positrons annihilate within the bulk-like regions before reaching the grain boundaries. This shift results in an increase in $I_1$ and a corresponding decrease in $I_2$.

Although the average positron lifetime, $\tau_{avg}$, changes with increasing $Sc^{3+}$ content (Fig. 6c), this should not be taken as a direct indication of altered defect concentration. The individual lifetime components, $\tau_1$ and $\tau_2$, remain nearly constant, indicating that the nature and size of annihilation sites do not significantly change. Instead, variations in $\tau_{avg}$ mainly result from changes in the relative intensities $I_1$ and $I_2$, which represent the fraction of positrons annihilating in the crystal bulk *versus* vacancy clusters near grain boundaries. Due to the change in crystallite size with $Sc^{3+}$ doping, it is difficult to separate positron trapping at specific defects from general annihilation influenced by crystallite size. Therefore, the decrease in $\tau_{avg}$ with increasing $Sc^{3+}$ content is mainly driven by microstructural effects – specifically the spatial distribution of annihilation sites – rather than a reduction in defect concentration.

**3.3.4. $GdVO_4$:Yb/Er/Cd.** Doping with $Cd^{2+}$ ions leads to distinct modifications in the positron annihilation characteristics. As the $Cd^{2+}$ concentration increases from 5% to 15%, the shortest positron lifetime component, $\tau_1$, rises considerably, reaching approximately 213 ps at 15% Cd (Fig. 6a). This value closely matches the theoretically predicted positron lifetime for isolated Gd monovacancies (V_Gd) (Fig. 6a and Table S1), indicating that $Cd^{2+}$ substitution for $Gd^{3+}$ strongly promotes the formation of Gd vacancies, which become the dominant positron trapping sites. Even at 5% Cd, the increase in $\tau_1$ is already significant, suggesting that the introduction of $Cd^{2+}$ efficiently alters the defect landscape by encouraging monovacancy formation. Due to the pronounced dominance of V_Gd, distinguishing the specific roles of dislocations or V_O is challenging, and any estimation of their contributions remains uncertain. Additionally, the microstrain, as measured by XRD, decreases with increasing Cd content, implying a reduction in dislocation density or increased mobility and annihilation of extended defects.

The second positron lifetime component, $\tau_2$, associated with larger vacancy clusters or extended open-volume defects, increases to 406 ps at 5% Cd, which is characteristic of large Gd vacancy clusters such as $>V_{20}$_Gd, Table S1, but this size is considered a rough estimate since the exact cluster geometry has an influence on the open volume and therefore calculated lifetime. At 15% Cd, $\tau_2$ decreases to a value indicative of smaller clusters close to the reference sample (390 ps for $\sim V_{20}$_Gd), suggesting a possible recombination or fragmentation of vacancy clusters as the Cd content increases. The intensity parameters $I_1$ and $I_2$ also evolve with Cd doping: $I_1$ increases at 5% Cd, reflecting a greater proportion of positrons annihilating in monovacancies, while $I_2$ decreases, indicating a reduced fraction of positron annihilation in larger vacancy clusters. This behavior persists at 15% Cd doping; however, the increase in $I_1$ does not scale proportionally with Cd content, indicating that the formation of Gd monovacancies occurs in a nonlinear manner with respect to $Cd^{2+}$ concentration.

The average positron lifetime, $\tau_{avg}$, decreases with Cd doping almost linearly (Fig. 6c). Crucially, XRD analysis shows that the crystallite size remains nearly constant at approximately 80 nm for both 5% and 15% Cd-doped samples. This constancy confirms that the variations observed in positron annihilation parameters – particularly in $\tau_{avg}$ – are indicative of intrinsic modifications in the defect structure. It further suggests that the overall defect density decreases with increasing Cd content, primarily due to a reduction in the density of defect clusters located at grain boundaries.

**3.3.5. $GdVO_4$:Yb/Er/Zn.** The defects of $GdVO_4$:Yb/Er co-doped with $Zn^{2+}$ display distinctive characteristics when compared to both the undoped material and the case of $Cd^{2+}$ co-doping, a chemically similar dopant with the same oxidation state. Despite their shared divalent nature, the $Zn^{2+}$-doped system shows a notably different positron annihilation signature. The $\tau_1$ value stabilizes around 205 ps across $Zn^{2+}$ concentrations, which is lower than the calculated value for isolated Gd monovacancies (V_Gd $\approx$ 216.5 ps, Fig. 6a and Table S1). This suggests that $\tau_1$ reflects a combined contribution from V_Gd and additional residual defects. Specifically, $\tau_1$ may include annihilation at V_O and residual dislocations – both of which yield shorter positron lifetimes than V_Gd and thus prevent $\tau_1$ from reaching its expected upper bound. The contribution from dislocations becomes minimal at 15% $Zn^{2+}$ doping, as evidenced by the reduced residual crystal microstrain observed in XRD ($1.2 \pm 0.7 \times 10^{-3}$), further implying that V_O is the primary remaining contributor influencing $\tau_1$ at high $Zn^{2+}$ content. Yet, its specific effect cannot be satisfactorily disentangled.

A key difference in $Zn^{2+}$ co-doping emerges in the defect cluster behavior. The $\tau_2$ component exhibits a marked decrease with increasing $Zn^{2+}$ concentration, reflecting a progressive reduction in the size of vacancy clusters at grain boundaries.

This decline results in $\tau_2$ values that are even shorter than those measured in undoped $GdVO_4$, indicating a significant suppression of defect clustering.

Regarding intensities, both $I_1$ and $I_2$ change with Zn content, but these variations can be largely attributed to the increase in crystallite size, which grows from approximately 30 nm in the undoped sample to 78 nm at 5% Zn and 88 nm at 15% Zn. Larger crystallites enhance the probability that positrons annihilate within the bulk, thereby increasing $I_1$ and reducing $I_2$, which corresponds to positron annihilation at vacancy clusters near grain boundaries. This microstructural effect must be considered alongside defect evolution when interpreting intensity changes.

The decreasing $\tau_{avg}$ must be treated with caution. While the reduction in $\tau_{avg}$ may suggest a decrease in overall defect density, it also reflects a shift in the nature and size of the trapping sites. Given the strong influence of crystallite size on intensity components, it is not possible to unambiguously attribute this trend to a lower total defect density, like in the $Sc^{3+}$ case. However, the consistent decline in $\tau_2$ suggests that large defect clusters become smaller with Zn co-doping.

## 4. Discussion

The present study shows that the luminescence performance is closely linked to complex defect microstructures within the host lattice. Using PALS, we systematically investigate defect characteristics in $GdVO_4$ doped with various ions – $Yb^{3+}$/$Er^{3+}$, $Sc^{3+}$, $Cd^{2+}$, and $Zn^{2+}$. These dopants were chosen to systematically explore the influence of dopant valence and ionic radius on defect formation and luminescent properties. Complementary XRD and SEM analyses provide insights into structural and morphological evolution during doping. Our results reveal that defect formation is strongly influenced by dopant valence and ionic radius, leading to distinct microstructural patterns. By correlating these findings with PLQY measurements, we establish clear structure–defect–property relationships, offering guidance for the targeted design of efficient UC materials. This section aims to explicitly detail these structure–defect–property relationships, particularly focusing on how specific defect characteristics influence the observed PLQY trends.

By combining PALS results with structural characterization by XRD, the following table can be provided. The data in Table 3 indicate that dopant valence strongly influences defect types: isovalent ions ($Yb^{3+}$, $Er^{3+}$, $Sc^{3+}$) mainly cause lattice strain, while aliovalent dopants ($Cd^{2+}$, $Zn^{2+}$) induce additional charge compensation defects. Ionic size mismatch drives defect formation, especially oxygen vacancies (V_O), with larger mismatches increasing defect prevalence. Crystallite size affects positron annihilation sensitivity – small crystallites ($\sim$29 nm) enhance defect detection at boundaries, whereas larger ones ($\sim$88 nm) favor bulk annihilation signals.

For a comparative analysis over the samples and to link the structural defects to the PQLY, one observes the PLQY trend: $Cd^{2+}$ < $Sc^{3+}$ < $Zn^{2+}$ (lowest → highest), as summarized in Table 3. This observed trend is directly correlated with the distinct defect microstructures and their impact on radiative and non-radiative recombination pathways, as elaborated below:

(i) Charge compensation and vacancy type: aliovalent doping with $Cd^{2+}$ and $Zn^{2+}$ leads to the formation of Gd vacancies (V_Gd), while $Sc^{3+}$, being isovalent, does not induce such defects. However, PLQY trends do not correlate directly with vacancy presence. Although $Zn^{2+}$ introduces V_Gd, it exhibits the highest PLQY – highlighting that the type and arrangement of defects, rather than their presence alone, is crucial.

(ii) Defect cluster size and distribution: a major distinguishing factor is the extent of defect clustering. $Cd^{2+}$-doped samples show the formation of large, spatially extended V_Gd clusters, which act as efficient non-radiative quenching centers, thereby suppressing PLQY. In contrast, $Zn^{2+}$ shows a marked suppression in defect cluster growth, leading to smaller defect sites that reduce quenching. This cluster suppression appears to be the key factor governing the improved PLQY in Zn.

(iii) Grain boundary *vs.* crystallite contributions: PALS data suggest that $Zn^{2+}$ may additionally favor the localization of beneficial oxygen vacancies (V_O) within crystallite interiors rather than at boundaries, while simultaneously minimizing extended defect structures at grain interfaces. This spatial redistribution of defects supports radiative recombination pathways and further boosts luminescence efficiency.

(iv) Scandium case – minimal point defects but clustered vacancies: although $Sc^{3+}$-doped samples show defect clusters of comparable size to $Cd^{2+}$ at high co-doping levels, their PLQY is significantly better. This improvement can be attributed to the lack of point defects like V_Gd and V_O and a more compact, structurally ordered lattice, which compensates for the quenching effect of vacancy clusters and supports moderately efficient light emission.

To this end, the superior PLQY observed in Zn-doped $GdVO_4$ can be primarily attributed to the suppression of defect cluster formation, which drastically reduces non-radiative recombination. Additionally, a favorable distribution of oxygen vacancies inside the crystallites, rather than at grain boundaries, may contribute synergistically. These effects outweigh the influence of microstrain or simple vacancy presence.

Table 3 Individual system characteristics as deduced from PALS and XRD results

| Doping system | Primary defects | Key evolution pattern | Cluster behavior | Crystallite size | PLQY trend |
|---|---|---|---|---|---|
| $GdVO_4$:Yb/Er | V_O dominant | Size mismatch → V_O formation | $V_{20}$_Gd clusters | 29 nm | Baseline |
| $GdVO_4$:Yb/Er/Sc | V_O suppressed | Lattice contraction → V_O elimination | Clusters unchanged | 30 → 51 nm | ↑ |
| $GdVO_4$:Yb/Er/Cd | V_Gd dominant | Charge compensation → strong V_Gd | > V_20 → $V_{20}$_Gd fragmentation | ∼80 nm | ↓ |
| $GdVO_4$:Yb/Er/Zn | V_Gd + V_O mixed | Partial charge compensation | Progressive cluster suppression | 78 → 88 nm | ↑↑ |

 

## 5. Conclusions

This study provides a mechanistic understanding of how co-doping strategies influence the UC performance of $GdVO_4$:$Yb^{3+}$/$Er^{3+}$ microcrystals by modulating their defect landscape. Through a detailed comparison of isovalent and aliovalent co-doping approaches, it becomes evident that not the mere presence of defects, but their spatial arrangement and clustering behavior, critically governs the PLQY. Beyond the well-established roles of ionic radius and valence, our findings suggest that the topology of defects – including their spatial distribution, connectivity, and cluster size – plays a decisive role in determining UC efficiency.

PALS, alongside X-ray diffraction and optical measurements, reveals that aliovalent dopants such as $Cd^{2+}$ and $Zn^{2+}$ introduce charge imbalance that is compensated by the formation of Gd vacancies. However, the structural response to this compensation varies significantly between the two systems. In the case of $Cd^{2+}$ co-doping, charge compensation leads to the formation of large and spatially extended vacancy clusters, potentially concentrated at grain boundaries. These clusters act as effective non-radiative recombination centers, significantly quenching the UC emission and resulting in low PLQY. Despite exhibiting relatively low microstrain, the defect morphology in the $Cd^{2+}$ system remains detrimental due to the high degree of defect clustering.

By contrast, $Zn^{2+}$ co-doping results in a markedly different defect structure. Although similar charge compensation mechanisms are at play, the $Zn^{2+}$-doped system suppresses the expansion of vacancy clusters, leading to more confined and less interconnected defect configurations. This refined cluster morphology reduces the density of non-radiative quenching sites, particularly at grain interfaces, while potentially preserving optically active oxygen vacancies within the crystallites. The resulting defect topology enables a more favorable radiative-to-nonradiative recombination balance and corresponds to the highest observed PLQY among the systems investigated.

The case of $Sc^{3+}$ co-doping offers a contrasting scenario where no charge compensation is required. The absence of aliovalent substitution leads to a more compact lattice with negligible formation of point defects. While defect clusters persist – likely remnants from synthesis or structural relaxation – they are not accompanied by high internal strain or deep trapping states. Consequently, the PLQY in the $Sc^{3+}$ system is superior to that of $Cd^{2+}$-doped samples but remains lower than in $Zn^{2+}$ due to the lack of beneficial oxygen vacancies and the persistence of moderate-sized clusters.

Isovalent co-doping with $Bi^{3+}$ and $In^{3+}$ – both of which possess larger ionic radii compared to $Sc^{3+}$ – leads to the formation of larger microcrystals with reduced lattice strain. This structural modification contributes to an increase in PLQY at lower doping concentrations (5%). However, at higher doping levels (15%), the PLQY values remain comparable across all three dopants: $Sc^{3+}$, $Bi^{3+}$, and $In^{3+}$.

Overall, the findings demonstrate that optimizing UC performance is not simply a matter of reducing total defect density, but rather of engineering the size, location, and distribution of defect clusters within the microstructure. $Zn^{2+}$ co-doping achieves the most advantageous configuration by combining efficient charge compensation with spatial control over defect clustering and potential redistribution of optically beneficial defects. These mechanistic insights underscore the importance of targeted defect engineering in the design of efficient UC materials and establish PALS as a critical technique for decoding the structure–luminescence relationships at the nanoscale.

## Conflicts of interest

There are no conflicts to declare.

## Data availability

The supplementary information (SI) describes the calculation of crystallite size and microstrain, as well as the UC luminescence spectra and PALS modelling. See DOI: **https://doi.org/10.1039/d5tc03342j**.

The data that support the findings of this study are available from the corresponding author upon reasonable request.

## Acknowledgements

The financial support provided by the Helmholtz Association is gratefully acknowledged: (i) a Recruitment Initiative Fellowship for B. S. R.; (ii) the funding of chemical synthesis equipment from the Helmholtz Materials Energy Foundry (HEMF); and (iii) Research Field Energy – Program Materials and Technologies for the Energy Transition – Topic 1 Photovoltaics (38.01.02).

## References

1 Z. Lv, H. Xu, Z. Wang, M. Jia, Y. Wei and Z. Fu, *J. Alloys Compd.*, 2021, **894**, 162298.
2 G. Tessitore, G. A. Mandl, S. L. Maurizio, M. Kaur and J. A. Capobianco, *RSC Adv.*, 2023, **13**, 17787–17811.
3 Q.-C. Sun, Y. C. Ding, D. M. Sagar and P. Nagpal, *Prog. Surf. Sci.*, 2017, **92**, 281–316.
4 B. S. Richards, D. Hudry, D. Busko, A. Turshatov and I. A. Howard, *Chem. Rev.*, 2021, **121**, 9165–9195.
5 S. Wang, J. Feng, S. Song and H. Zhang, *CrystEngComm*, 2013, **15**, 7142–7151.
6 E. M. Mettenbrink, W. Yang and S. Wilhelm, *Adv. Photonics Res.*, 2022, **3**, 2200098.
7 H. Li, H. Liu, K. L. Wong and A. H. All, *Biomater. Sci.*, 2024, **12**, 4650–4663.
8 R. Singh, E. Madirov, D. Busko, I. M. Hossain, V. A. Konyushkin, A. N. Nakladov, S. V. Kuznetsov, A. Farooq, S. Gharibzadeh, U. W. Paetzold, B. S. Richards and A. Turshatov, *ACS Appl. Mater. Interfaces*, 2021, **13**, 54874–54883.
9 J. C. Goldschmidt and S. Fischer, *Adv. Opt. Mater.*, 2015, **3**, 510–535.

10 Y. Wu, S. Y. Chan, J. Xu and X. Liu, *Chem. – Asian J.*, 2021, **16**, 2596–2609.
11 P. Dash, P. K. Panda, C. Su, Y. C. Lin, R. Sakthivel, S. L. Chen and R. J. Chung, *J. Mater. Chem. B*, 2024, **12**, 3881–3907.
12 H. Suo, Q. Zhu, X. Zhang, B. Chen, J. Chen and F. Wang, *Mater. Today Phys.*, 2021, **21**, 100520.
13 B. Xue, D. Wang, L. Tu, D. Sun, P. Jing, Y. Chang, Y. Zhang, X. Liu, J. Zuo, J. Song, J. Qu, E. J. Meijer, H. Zhang and X. Kong, *J. Phys. Chem. Lett.*, 2018, **9**, 4625–4631.
14 Z. Wang and A. Meijerink, *J. Phys. Chem. C*, 2018, **122**, 26298–26306.
15 F. T. Rabouw, P. T. Prins, P. Villanueva-Delgado, M. Castelijns, R. G. Geitenbeek and A. Meijerink, *ACS Nano*, 2018, **12**, 4812–4823.
16 Y. Feng, Z. Li, Q. Li, J. Yuan, L. Tu, L. Ning and H. Zhang, *Light:Sci. Appl.*, 2021, **10**, 1–10.
17 E. I. Madirov, V. A. Konyushkin, A. N. Nakladov, P. P. Fedorov, T. Bergfeldt, D. Busko, I. A. Howard, B. S. Richards, S. V. Kuznetsov and A. Turshatov, *J. Mater. Chem. C*, 2021, **9**, 3493–3503.
18 D. Hudry, A. De Backer, R. Popescu, D. Busko, I. A. Howard, S. Bals, Y. Zhang, A. Pedrazo-Tardajos, S. Van Aert, D. Gerthsen, T. Altantzis and B. S. Richards, *Small*, 2021, **17**, 2104441.
19 A. Chauhan, S. Kataria, D. Busko, F. A. Cardona, A. Turshatov and B. S. Richards, *J. Mater. Chem. C*, 2021, **9**, 16709–16720.
20 U. Resch-Genger and H. H. Gorris, *Anal. Bioanal. Chem.*, 2017, **409**, 5855–5874.
21 M. Chaika, R. Tomala, O. Vovk, S. Nizhankovskyi, G. Mancardi and W. Strek, *J. Lumin.*, 2020, **226**, 117467.
22 F. Auzel, *Chem. Rev.*, 2004, **104**, 139–173.
23 Y. Niihori, T. Kosaka and Y. Negishi, *Mater. Horiz.*, 2024, **11**, 2304–2322.
24 S. K. W. MacDougall, A. Ivaturi, J. Marques-Hueso, K. W. Krämer and B. S. Richards, *Opt. Express*, 2012, **20**, A879–A887.
25 S. Gai, C. Li, P. Yang and J. Lin, *Chem. Rev.*, 2014, **114**, 2343–2389.
26 J. H. Oh, B. K. Moon, B. C. Choi, J. H. Jeong, J. H. Kim and H. S. Lee, *Solid State Sci.*, 2015, **42**, 1–5.
27 O. A. Savchuk, J. J. Carvajal, C. Cascales, M. Aguiló and F. Díaz, *ACS Appl. Mater. Interfaces*, 2016, **8**, 7266–7273.
28 Y. Liang, H. M. Noh, J. Xue, H. Choi, S. H. Park, B. C. Choi, J. H. Kim and J. H. Jeong, *Mater. Des.*, 2017, **130**, 190–196.
29 Y. Niyom, E. Madirov, N. M. Bhiri, A. Chauhan, B. S. Richards, A. Flood, D. Crespy and A. Turshatov, *Opt. Mater.*, 2023, **140**, 113833.
30 E. L. Cates, A. P. Wilkinson and J. H. Kim, *J. Phys. Chem. C*, 2012, **116**, 12772–12778.
31 M. Liu, P. Diercks, A. Manzoni, J. Čížek, U. Ramamurty and J. Banhart, *Acta Mater.*, 2021, **220**, 117298.
32 J. Čížek, *J. Mater. Sci. Technol.*, 2018, **34**, 577–598.
33 D. Zhou, L. X. Pang, D. W. Wang and I. M. Reaney, *J. Mater. Chem. C*, 2018, **6**, 9290–9313.
34 S. C. Abrahams, K. Nassau, J. Ravez, A. Simon and R. Olazcuaga, *J. Appl. Crystallogr.*, 1983, **16**, 133–135.
35 O. Voloshyna, M. V. Gorbunov, D. Mikhailova, A. Maljuk, S. Seiro and B. Büchner, *Crystals*, 2023, **13**, 1439.
36 A. Dupasquier and A. P. Mills, *Positron spectroscopy of solids*, IOS, Ohmsha, 1995.
37 P. Hautojärvi and A. Vehanen, *Positron in Solids*, Springer, Berlin, Heidelberg, 1979.
38 R. Krause-Rehberg and H. S. Leipner, *Positron Annihilation in Semiconductors: Defect Studies*, Springer-Verlag, Berlin, Heidelberg, 1st edn, 1999.
39 M. Elsayed, T. E. M. Staab, J. Čížek and R. Krause-Rehberg, *Acta Mater.*, 2023, **248**, 118770.
40 M. Rappaz, L. A. Boatner and M. M. Abraham, *J. Chem. Phys.*, 1980, **73**, 1095–1103.
41 J. Hu, J. Zhang, H. Zhao, Y. Mao, J. Zhang, L. Lin, N. Y. Garces, K. T. Stevens, G. K. Foundos and L. E. Halliburton, *J. Phys.: Condens. Matter*, 2004, **16**, 7095.
42 P. T. Hue, N. T. N. Hue, N. Van Tiep, N. V. M. Trung, P. T. Phuc, L. L. Nguyen, L. T. Son, L. T. Q. Trang, N. D. Trung, N. Q. Hung, L. A. Tuyen and N. H. Duy, *Luminescence*, 2024, **39**, 1522–7235.
43 L. N. Akay, S. Kuzeci, N. Akti, M. Erdem, C. Tav, U. Yahsi, G. Eryurek and B. Di Bartolo, *ECS J. Solid State Sci. Technol.*, 2023, **12**, 086005.
44 A. Siva Sesha Reddy, M. Kostrzewa, V. Ravi Kumar, A. Ingram, N. Venkatramaiah, G. Sahaya Baskaran, V. Ravi Kumar and N. Veeraiah, *Luminescence*, 2022, **37**, 1776–1784.
45 L. K. Andersen, T. J. Morgan, A. K. Boulamanti, P. Álvarez, S. V. Vassilev and D. Baxter, *Energy Fuels*, 2013, **27**, 7439–7454.
46 E. Hirschmann, M. Butterling, U. Hernandez Acosta, M. O. Liedke, A. G. Attallah, M. P. Petring, M. M. Görler, R. Krause-Rehberg and A. Wagner, *J. Instrum.*, 2021, **16**, P08001.
47 Z. Ma, P. Monalisha, Z. Tan, E. Pellicer, M. O. Liedke, M. Butterling, A. G. Attallah, E. Hirschmann, A. Wagner, F. Ibrahim, M. Chshiev, E. Men Endez and J. Sort, *J. Materiomics*, 2024, **10**, 870–879.
48 D. Nath, F. Singh and R. Das, *Mater. Chem. Phys.*, 2020, **239**, 122021.
49 E. Madirov, D. Busko, F. A. Cardona, D. Hudry, S. V. Kuznetsov, V. A. Konyushkin, A. N. Nakladov, A. A. Alexandrov, I. A. Howard, B. S. Richards and A. Turshatov, *Adv. Photonics Res.*, 2023, **4**, 2200187.
50 J. V. Olsen, P. Kirkegaard, N. J. Pedersen and M. Eldrup, *Phys. Status Solidi C*, 2007, **4**, 4004–4006.
51 R. N. West, *Adv. Phys.*, 1973, **22**, 263–383.
52 Z. Wu, D. Chaykina, H. Schreuders, H. Schut, M. De Boer, M. O. Liedke, M. Butterling, A. Wagner, M. Dickmann, E. Brück, B. Dam and S. W. H. Eijt, *Phys. Rev. Mater.*, 2025, **9**, 015201.
53 R. Auguste, H. L. Chan, E. Romanovskaia, J. Qiu, R. Schoell, M. O. Liedke, M. Butterling, E. Hirschmann, A. G. Attallah, A. Wagner, F. A. Selim, D. Kaoumi, B. P. Uberuaga,

 

P. Hosemann and J. R. Scully, *npj Mater. Degrad.*, 2022, **6**, 1–13.
54 E. Boroński and R. M. Nieminen, *Phys. Rev. B:Condens. Matter Mater. Phys.*, 1986, **34**, 3820.
55 A. P. Seitsonen, M. J. Puska and R. M. Nieminen, *Phys. Rev. B:Condens. Matter Mater. Phys.*, 1995, **51**, 14057.
56 M. J. Puska and R. M. Nieminen, *J. Phys. F: Met. Phys.*, 1983, **13**, 333.
57 H. Häkkinen, S. Mäkinen and M. Manninen, *Europhys. Lett.*, 1989, **9**, 809.
58 Z. Q. Chen, X. W. Hu and S. J. Wang, *Phys. Status Solidi A*, 1996, **156**, 277–284.